Design and Analysis of a Frequency Selective Surface Loaded Bioinspired Antenna in Frequency and Time Domains

Anett Antony* **and Bidisha Dasgupta**

Abstract—The paper addresses a bioinspired printed antenna in the shape of a 'Lotus' which is further loaded with a new type of Frequency Selective Surface (FSS) structure with unit cell dimension as $0.16\lambda_0 \times 0.16\lambda_0 \times 0.033\lambda_0$, where λ_0 is the lowest operating wavelength. The two dissimilar layers of FSS, which are separated by an air gap of about 3.2 mm, have been placed below the antenna. The combined structure operates over 3.8 GHz to 14.4 GHz (116.5% measured) with peak realized gain of 7.5 dBi. The introduction of the FSS layer provides gain enhancement of about 5.9 dBi. The stand-alone FSS geometry provides a wide transmission bandwidth from 5.5 to 12.5 GHz along with good angular stability of about 50°. The Gielis superformula has been used to develop the petal of the lotus shaped antenna. The time domain analysis of the lotus shaped antenna has also been provided. The proposed structure can be used as an electromagnetic sensor for wide band applications over C, X, and partially Ku bands.

1. INTRODUCTION

Frequency Selective Surface (FSS) technology has been explored over the past few decades [1, 2], and the development extends from simple geometries to complex structures for numerous applications in various fields such as aerospace, medicine, microwave industry, and real estate [1]. FSSs are sub-wavelength type repeating structures which in the field of microwave antennas, are generally used as a superstrate or as a high impedance ground plane to enhance the gain, bandwidth, and to reduce the out-of-band radar cross section of the antenna [1–3]. The use of metallic reflector in various forms was a conventional way to improve the directional gain of the antenna, but it was found that if the space between antenna and reflector was less than a quarter wavelength, then image currents would cancel each other which resulted in poor radiation efficiency [3], and the metallic reflector also caused out of band scattering due to decreased selectivity. To overcome these problems, periodic structures like partially reflective surfaces (PRS) [4, 5] and FSS [2] can be used to improve the gain of the antenna. Although a single layer of FSS has its own advantages like easy fabrication, it is inefficient due to its unstable performance with the variation of electromagnetic (EM) wave incident angle and decreased bandwidth [6]. On the other hand, multi-layered complex FSS structures achieve a wideband response as shown by the authors in [7–9] and also stability under oblique incidence as shown in [8, 9] in the desired frequency range. However, significant precision is required to manufacture multilayer FSS. In [7], the authors have proposed a two-layer FSS which works over the ultra-wideband (UWB), but the authors have not discussed the stability of the FSS under oblique incidence which is an important parameter while designing FSS. In [8], the authors have proposed a Dielectric Resonator Antenna (DRA) loaded with a double sided FSS which operates over the X band, but due to the use of DRA the bulkiness of the structure is increased. On the other hand, with the advancement of wireless technology, the demand for UWB antennas which

can support more speed and higher bandwidth is increasing day by day. Among UWB antenna family, microstrip patch antennas are the popular candidates of interest due to their numerous advantages like low cost, easy fabrication, conformal to planar structures, light weight, and many more [10]. Bioinspired antennas are a new class of antennas which are designed using the shapes found in nature, to obtain more compact and efficient antennas.

In order to describe mathematically the various shapes found in nature, the Gielis superformula was proposed by Gielis in 2003 [11]. Based on this, a few wide band antennas have been reported in past literature, like a ginkgo biloba leaf-shaped antenna, jasmine flower shaped antenna, tulip shaped antenna [12], etc. One of the advantages of such antennas is the increase in electrical length due to the increase in perimeter with reduction in total dimension hence acting like fractals [12]. Although there are a few works reported on UWB bioinspired antennas, they mostly focused on frequency domain analysis. While designing a UWB antenna, time domain analysis is equally important because it helps to cross verify whether the given antenna operates in practical scenarios as well [13]. While performing the time domain analysis, it was observed that a change in the source pulse width can drastically affect the time domain parameters [14], which has not been addressed in many past works. A systematic approach to choose the appropriate pulse width for a short monopole type of antenna ($\sigma/\tau > 1$, where σ is the pulse width, and τ is the transit time, i.e., the ratio of the antenna length to the speed of light in free space [15]) was provided in [16] and has been used in the present study, and further analysis of various time domain parameters has been carried out. One of the challenges of UWB antenna design is to maintain suitable gain over the wide bandwidth. One of the possible solutions is to use FSS along with the UWB antenna to improve the gain which was adopted in [5–9]. In this method, there are a few design challenges like to maintain compact size, to obtain insensitivity to changes in incidence as well as polarization angles, and to improve the gain over the wide bandwidth. In this paper, the authors have addressed these challenges. A new type of two layered FSS has been developed for the gain improvement of a bioinspired lotus shaped UWB antenna, as shown in Figure 1(a). To the best of the authors knowledge, in past research FSS has not been explored much to improve the performance characteristics of a bioinspired antenna, and this gap area is targeted by the authors in the present work. Also, the proposed model provides superior characteristics in terms of gain, compactness, and bandwidth in comparison to compact antennas as tabulated in Section 5. The development of the antenna geometry using Gielis superformula and its performance in both frequency and time domains are presented in Section 2. The development of the FSS and its analysis using transmission line equivalent circuit model is provided in Section 3. Section 4 describes the simulated and measured results of the FSS loaded antenna. Finally, Section 5 concludes the paper. The parametric studies and performance analysis of the antenna and FSS geometries are carried out using EM simulator HFSS (Ansys) [17], and the time domain analysis has been done using Dassault Systems' CST [18].
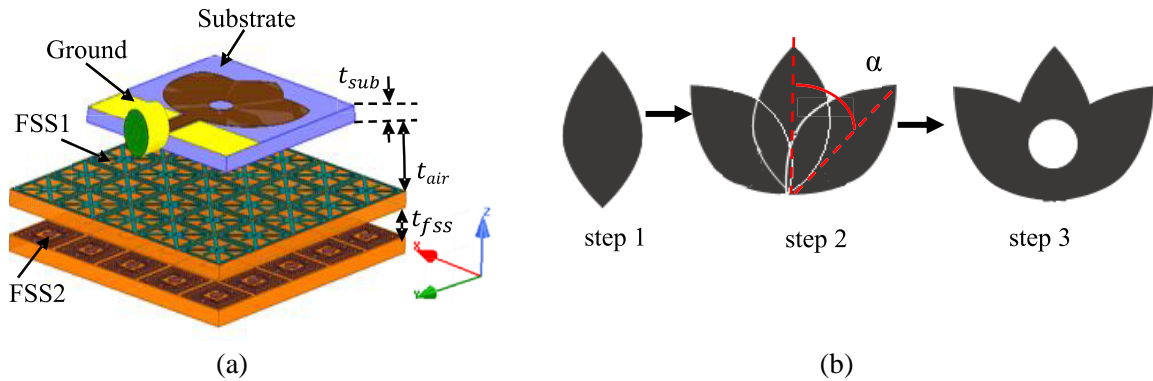

Figure 1. (a) Perspective view of antenna loaded with FSS, and (b) chronological development of the antenna geometry.

2. DEVELOPMENT OF THE STAND-ALONE ANTENNA GEOMETRY AND IT'S ANALYSIS IN FREQUENCY AND TIME DOMAINS

The antenna geometry has been developed using the Gielis superformula [11] in polar coordinates which is given as,

$$r\left(\varphi\right) = \cfrac{1}{\left\{ \left[\left(\left| \frac{1}{a} \cos\left(\frac{\varphi m}{4}\right) \right| \right)^{n2} + \left(\left| \frac{1}{b} \cos\left(\frac{\varphi m}{4}\right) \right| \right)^{n3} \right]^{\frac{1}{n1}} \right\}} \tag{1}$$

By assigning certain values to the six parameters, i.e., a, b, m, $n1$, $n2$, and $n3$, it is possible to develop and modify many shapes. When the values $a = 1$, $b = 1$, $m = 2$, $n1 = 1500$, $n2 = 1000$ and $n3 = 1000$ are assigned to Equation (1), a leaf (petal) shaped structure is obtained which is the initial structure used in this design. The structure is first generated using MATLAB in DXF format and then is imported into the full wave simulators [12]. The stand-alone leaf like geometry (Figure 1(b) step 1) operates over 2 to 11 GHz with $S_{11} < -8$ dB as shown in Figure 2(a), so the leaf shaped geometry is further left and right rotated by 45° (α) to obtain a lotus shaped structure (Figure 1(b) step 2) which operates from 1.8 GHz to 12.5 GHz ($S_{11} < -10$ dB). The S_{11} characteristics for different angles of rotation (α) of the leaf shaped patch are shown in Figure 2(b). In order to decrease high frequency ohmic losses, a circular slot is etched out of the lotus shaped patch structure (Figure 1(b) step 3). The labeled proposed antenna geometry and its dimensions are shown in Figure 3(a) and Table 1, respectively. A coplanar waveguide (CPW) type ground plane is used here. An alternative design approach for a nearly similar bioinspired antenna was reported by the authors in [19]. The proposed antenna operates from 1.8 GHz to 12.5 GHz with S_{11} minima at 3.5 GHz and 9.5 GHz and peak realized gain of about 1.65 dBi. The substrate used here is FR4 epoxy with dielectric constant (ε_s) = 4.4, loss tangent = 0.002, and thickness (t_{sub}) = 1.8 mm. The measured S_{11} is from 2.5 GHz to 13.2 GHz. A slight shift in the impedance bandwidth has been observed which can be due to loading. The simulated and measured radiation patterns are shown in Figure 3(b) for 6 GHz and 9.5 GHz, and the radiation pattern is approximately omnidirectional in nature in the $\Phi = 0°$ plane.
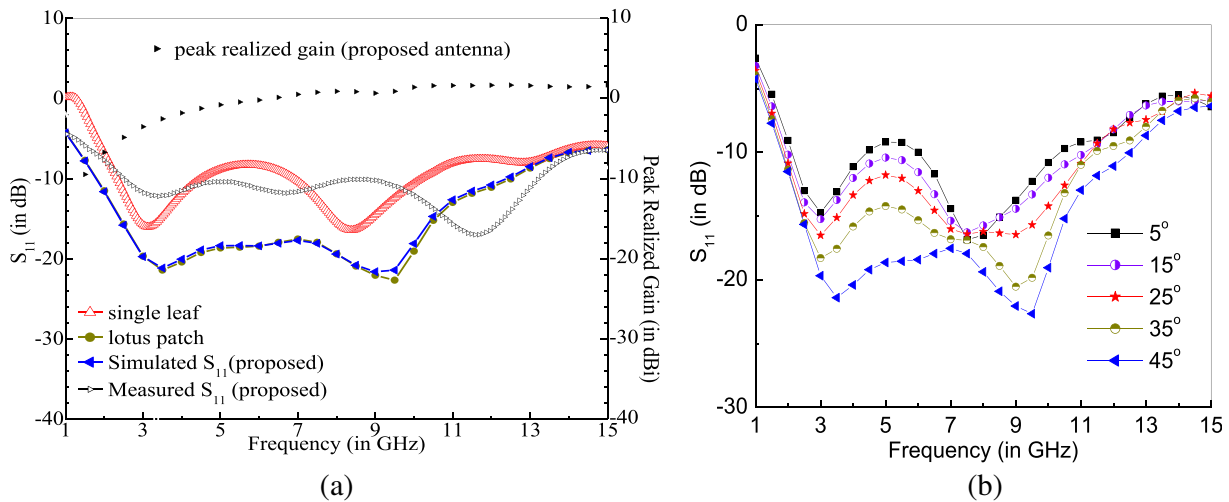

Figure 2. (a) Simulated S_{11} characteristics for different stages of the proposed antenna structure along with the measured S_{11} and simulated peak realized gain of the proposed antenna structure, and (b) simulated S_{11} characteristics for different α.

For the time domain analysis, monocycle pulse, which is the time derivative of the Gaussian pulse, has been used as the source signal because of its advantages like symmetric positive and negative sub-pulses with no inherent DC, compactness, and no inherent ringing [16]. The radiated electric field for monocycle pulses with different pulse widths is plotted in Figure 4(a). The monocycle pulses with

Table 1. Optimized design parameters of the proposed FSS loaded antenna (all dimensions are in mm).

w	l	w_g	l_g	t	g	d	t_{sub}	t_{fss}	t_{air}
30	31	13	8.25	3.1	0.4	4	1.8	3.2	7
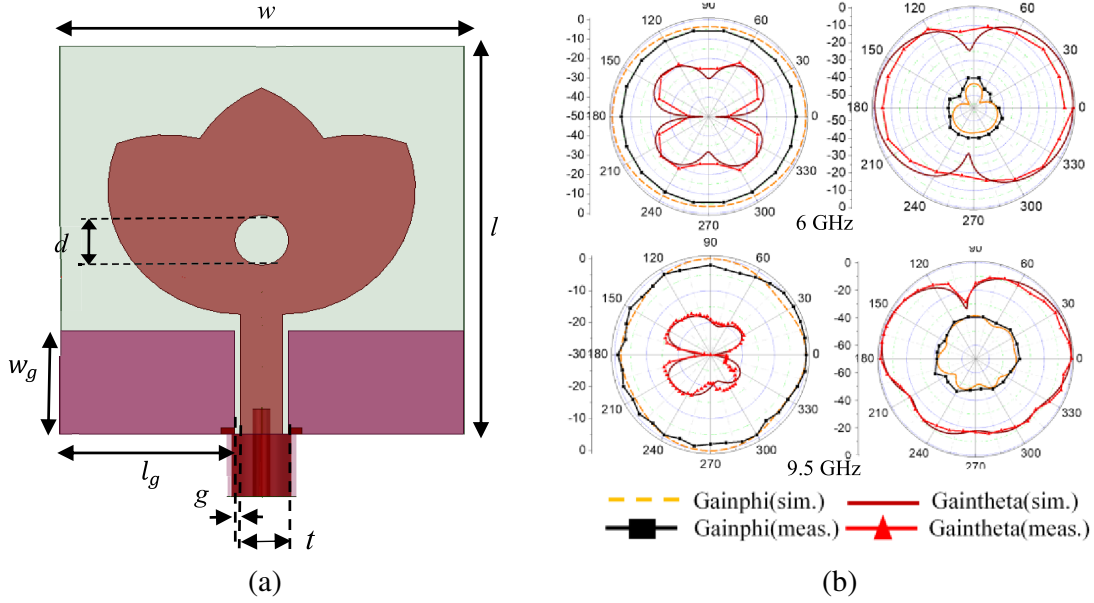
Figure 3. (a) Proposed antenna geometry (top view), and (b) simulated and measured radiation patterns of the antenna for $\Phi = 0°$ and $\Phi = 90°$ plane.
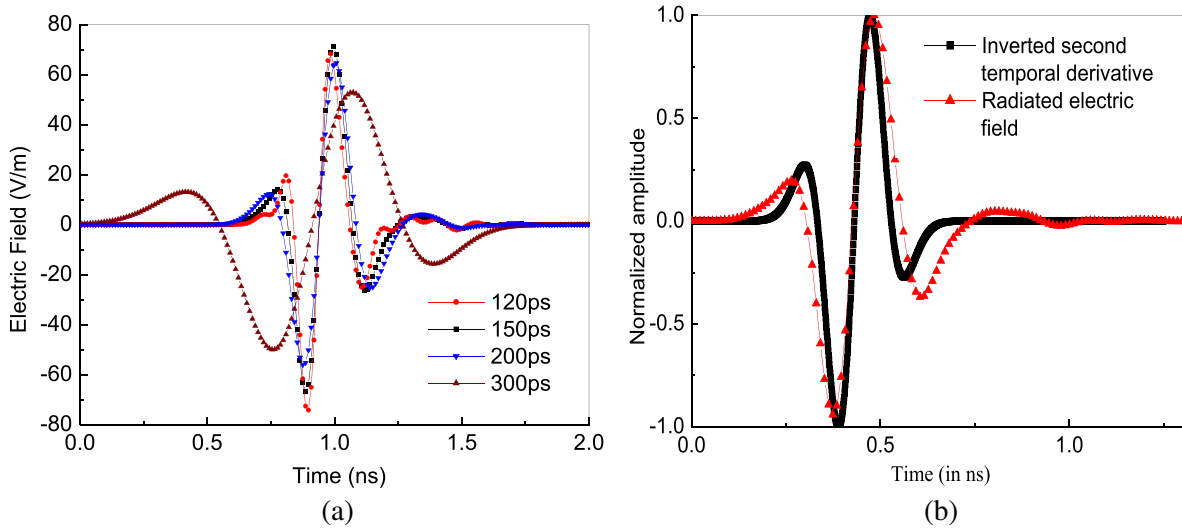
Figure 4. (a) Simulated radiated electric field for different widths of the monocycle pulse, and (b) comparison between the inverted second-order derivative of the monocycle pulse with 200 ps pulse width and the radiated electric field of the monocycle pulse with 200 ps pulse width.

pulse widths 150 ps and 200 ps have the radiated electric field response similar to the inverted second temporal derivative of the input monocycle pulse, as shown in Figure 4(b) (for 200 ps monocycle pulse), which satisfies the theoretical statement that a short dipole yields the second temporal derivative of the
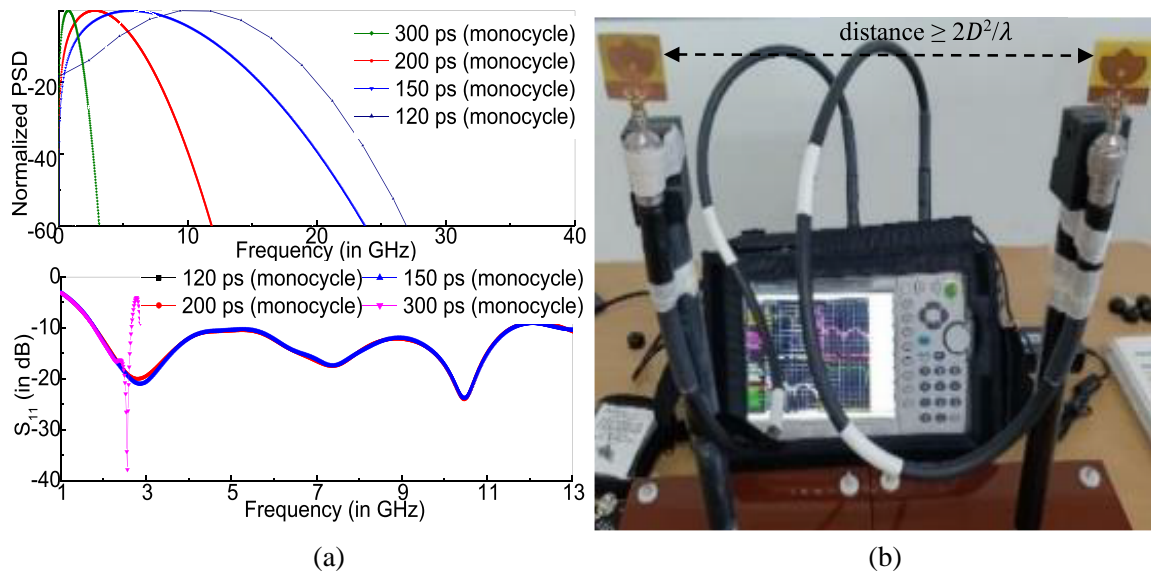
Figure 5. (a) Simulated normalized PSD (top) and simulated S_{11} characteristics (bottom) for different pulse widths of the monocycle pulse, and (b) measurement set up for side by side scenario.

input pulse [20]. The normalized power spectral density (PSD) and the S_{11} coefficient for different pulse widths of the monocycle pulses are shown in Figure 5(a). It can be observed that the larger the width of the pulse is in time domain, the smaller the area is occupied by that signal in the frequency domain. For a source signal to transmit over the whole band of operation, its PSD should cover the entire frequency band of the test antenna [16]. The monocycle pulses of width 200 ps, 150 ps, and 120 ps cover the entire operating bandwidth of the Antenna Under Test (AUT). However, the monocycle pulse of width 300 ps covers a very small portion of the operating band. The S_{11} characteristics reveal a similar fact that the response deteriorates for the monocycle pulse of width 300 ps. Therefore, the time domain parameters have been mainly studied using 150 ps and 200 ps monocycle pulses. For a distortionless reception, the magnitude of S_{21} should be a constant, and the phase of the S_{21} should be linear [21]. In order to obtain S_{21}, a setup having two similar antennas is used which are separated by a distance $\geq 2D^2/\lambda$, where D is the largest dimension, and λ is the wavelength corresponding to the highest operating frequency of the antenna. Here the antennas are placed in face to face and side by side scenarios. The measurement setup for side by side scenario is shown in Figure 5(b). The simulated S_{21} for both 150 ps and 200 ps monocycle pulses and measured S_{21} (both magnitude and phase) are shown in Figures 6(a) and (b), respectively, and it satisfies the above-mentioned criteria. Group delay is the frequency dependence of time delay [16]. A poor group delay can seriously affect a communication link [22]. The simulated group delays for 150 ps and 200 ps pulse widths of monocycle pulses and the measured group delay are plotted in Figure 6(c) for both the face to face and side by side scenarios. The maximum change in group delay is about 2 ns which is considered to be quite reasonable. The PSDs of the radiated pulses normalized to -41.3 dBm/MHz [23] for both 150 ps and 200 ps monocycle pulse widths are plotted in Figure 6(d). From the plot it can be observed that for both 150 ps and 200 ps monocycle pulse widths, the spectral density almost satisfies the FCC spectral limit. Ringing is the undesired ripples found along with the radiated signals. The ringing time is the time taken for the envelope function to fall from a peak value to α times its peak value, as depicted in Figure 7(a), where α is generally set as 0.22 [24]. As the energy spent in ringing is of no use, the ringing time should be negligibly small, i.e., of the order of a few hundred picoseconds. The ringing times for different pulse widths of the monocycle pulse are shown in Table 2. The width of the envelope is used to understand the phenomenon of pulse broadening. It is the time interval when the envelope reaches half of its maximum value, denoted as FWHM, as shown in Figure 7(a). To get high data rates or high resolution, the envelope width should be negligibly small, i.e., of the order of a few hundred picoseconds. The FWHMs for different pulse widths of the monocycle
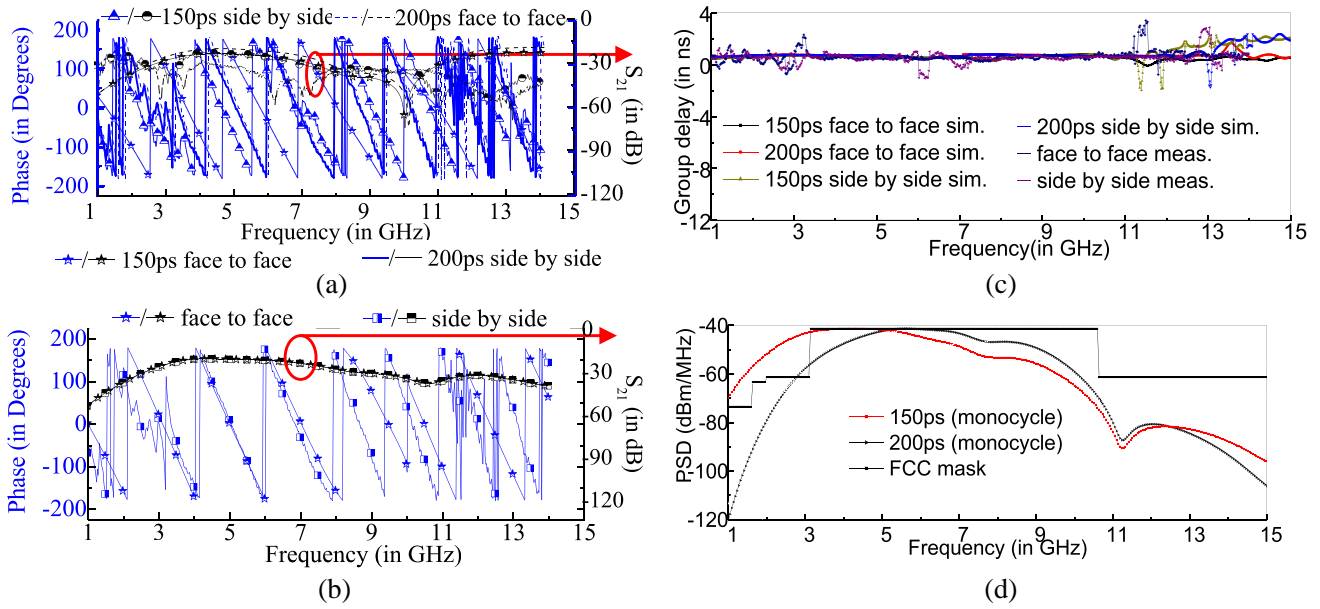
Figure 6. (a) Simulated S_{21} characteristics for different pulse widths and for different positions, (b) measured S_{21} characteristics for different positions, (c) simulated group delay (for different pulse width) and measured group delay for different positions and (d) radiated PSD characteristics.
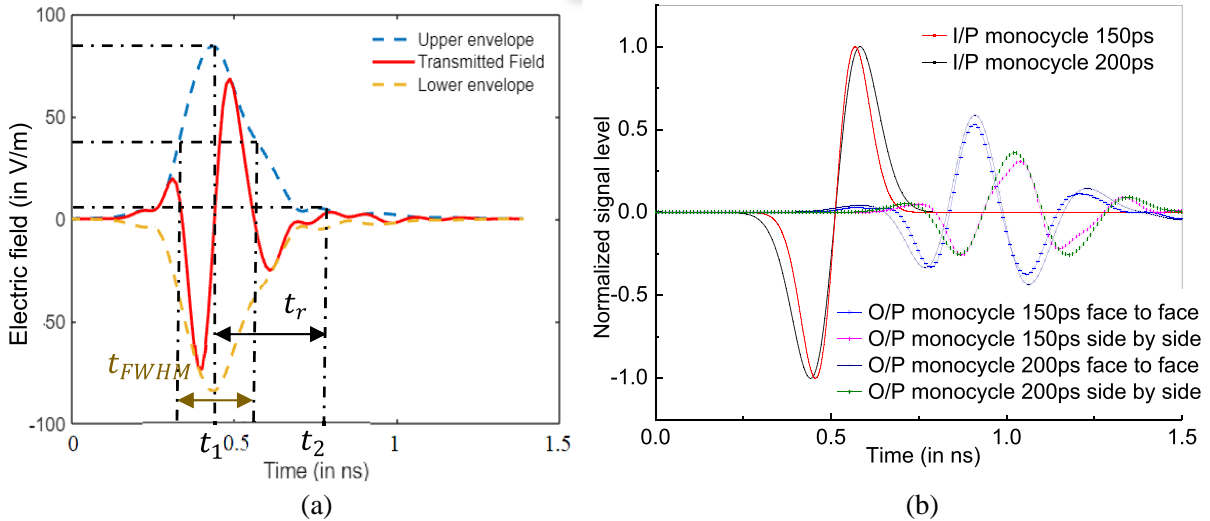

Figure 7. (a) Representation of ringing and envelope width, and (b) simulated input monocycle pulses and received pulses for face to face and side by side scenarios.

pulse are shown in Table 2. Both the ringing time and FWHM are acceptable for 150 ps and 200 ps monocycle pulses. Stretch ratio (SR) is used to find the temporal width of transmitted pulses. The pulse width for 90% of the energy capture is used to calculate SR, i.e., 5% energy in both the ends is removed [25]. For simplification the SR has been calculated for the $\Phi = 0°$ plane, as in this plane the radiation pattern is almost omnidirectional in nature as shown in Figure 3(b). Ideally, the value of SR should be 1. The SRs for different pulse widths of the monocycle pulses are tabulated in Table 2, for the transmitted pulses obtained from different angular positions of the antenna in the $\Phi = 0°$ plane. The SRs are acceptable for both 150 ps and 200 ps monocycle pulses. System Fidelity Factor (SFF) quantifies the level up to which the radiated electric field is correlated with the input signal voltage [25].

Table 2. Ringing, FWHM, SR and calculated SFF.

Pulse width	Ringing time	FWHM time	SR					Calculated SFF	
σ (ps)	$t_r = t_2 - t_1$ (ns)	t_{FWHM} (ns)	$0°$	$45°$	$90°$	$135°$	$180°$	Side by side	Face to face
150	0.187 (3.639–3.452)	0.2144	1.265	1.272	1.312	1.210	1.155	0.872	0.893
200	0.209 (3.661–3.452)	0.2638	1.327	1.318	1.320	1.330	1.320	0.885	0.887

If SFF value is 1, then the received signal pulse is identical to the input signal pulse at the transmitter; for value 0 the received signal is completely different from the transmitter input; and if it is less than 0.5 the received pulse becomes completely unrecognized. Table 2 shows the calculated SFFs for different pulse widths of the monocycle pulses. The SFFs are acceptable for both 150 ps and 200 ps monocycle pulses. The source signal and received signal for both face to face and side by side scenarios are plotted in Figure 7(b). The peak signal level decreases by 50% for the face to face scenario and by 66% for the side by side scenario.

3. DEVELOPMENT OF THE STAND-ALONE FSS GEOMETRY

In order to increase the gain of the bioinspired antenna over the operating bandwidth, one two-layered FSS structure is first designed and then introduced below the antenna structure. The requirement for FSS to act as a reflector is that its reflection coefficient S_{11} should be near 0 dB, and the transmission coefficient S_{12} should be less than -10 dB over the required band [7]. The FSS structure is initially started with a square loop element (SLE) because in a SLE, the interelement spacing is less than a patch type element which helps in providing increased transmission and reflection bandwidths and also delay the onset of grating lobes [8]. The approximate dimension of the SLE is calculated using the formula given below [8]

$$L_{\text{unit-cell}} = \frac{c}{2f_r\sqrt{(\varepsilon_s + 1)/2}} \tag{2}$$

Here c is the speed of light in vacuum in m/s, f_r the centre frequency (i.e., 8.5 GHz), and ε_s dielectric constant of the substrate. The top layer of the FSS structure is like a square-shaped ring with plus-cross and central circle (SSR-PCC) as shown in Figure 8(a), and the bottom layer is like a split multi-ring structure with a central circular patch (SMRS-CP), as shown in Figure 8(b). The dimensions are shown in the caption of Figure 8. Both the FSS structures have been developed using FR4 epoxy substrate with dielectric constant $(\varepsilon_s) = 4.4$, loss tangent $= 0.002$, and thickness $(t_{sub}) = 1.8$ mm. The top and bottom layers of the FSS are separated by an air gap ($t_{fss} = 3.2$ mm). The array used is 5×5 with 25
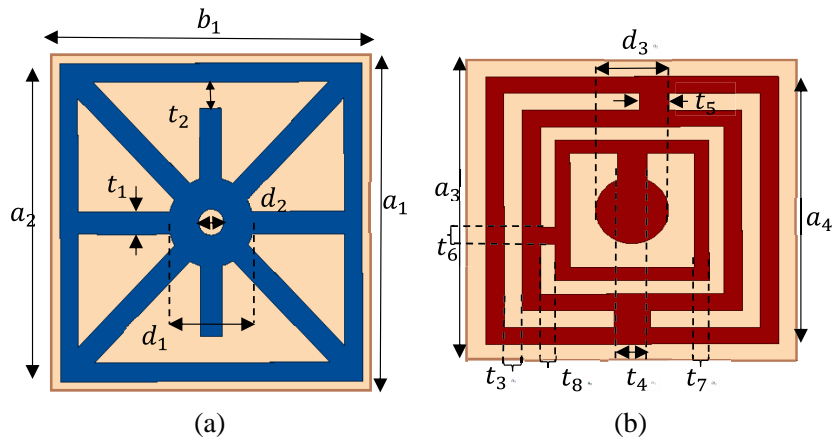

(a)   (b)

Figure 8. Proposed (a) top layer, and (b) bottom layer of FSS with dimensions given as $a_1 == 9$ mm, $b_1 = 9$ mm, $a_2 = 8.5$ mm, $t_1 = 0.6$ mm, $d_1 = 2.4$ mm, $t_2 = 0.7$ mm, $d_2 = 0.7$ mm, $a_3 = 9$ mm, $a_4 = 8$ mm, $d_3 = 2$ mm, $t_3 = 1$ mm, $t_4 = 0.8$ mm, $t_5 = 1$ mm, $t_6 = 0.8$ mm, $t_7 = 0.5$ mm, $t_8 = 0.8$ mm.

FSS unit cells (each having dimensions $9\,\text{mm} \times 9\,\text{mm} \times 1.8\,\text{mm}$, i.e., $0.16\lambda_0 \times 0.16\lambda_0 \times 0.033\lambda_0$) arranged periodically in both x and y directions. The transmission coefficient characteristics of the individual FSS layers and both FSS layers combined along with the reflection coefficient characteristics of the combined layer (to depict the non-absorbing characteristics) are depicted in Figure 9(a). The simulated transmission bandwidth obtained for the proposed FSS structure (i.e., both layers combined) is from 5.5 to 12.5 GHz, which is a very wide band. It is observed that both the FSS layers combined acts as a very good reflector with a very wide bandwidth. The structure is tested for stability under oblique incidence, and the response for TE polarization is shown in Figure 9(b). The FSS gives stable responses for angles up to $50°$. Simple structures did not provide angular stability over a wide bandwidth because of which a complex structure is developed. The discontinuity 't_2' provided in the top layer of FSS structure helps in providing angular stability in TE polarization. The improvement in angular stability achieved over the few initial stages during the development of the FSS structure for incidence angles $\theta = 0°$ and $\theta = 50°$ for TE polarization is shown in Figure 10(a). It is observed that the introduction of the second layer has improved the angular stability. Under normal incidence the change in polarization angle does not affect the transmission bandwidth of the proposed FSS structure as shown in Figure 10(b). The reflection phase characteristics of the proposed FSS are also shown in Figure 10(b). The grating lobes are undesirable feature in FSS because they degrade the FSS performance by taking part of the energy incident on the FSS [2]. The FSS unit cell has been designed using a small dimension so that the occurrence of the grating lobes can be minimized. The current distributions of the top and bottom layers of the FSS structure are shown in Figure 11.
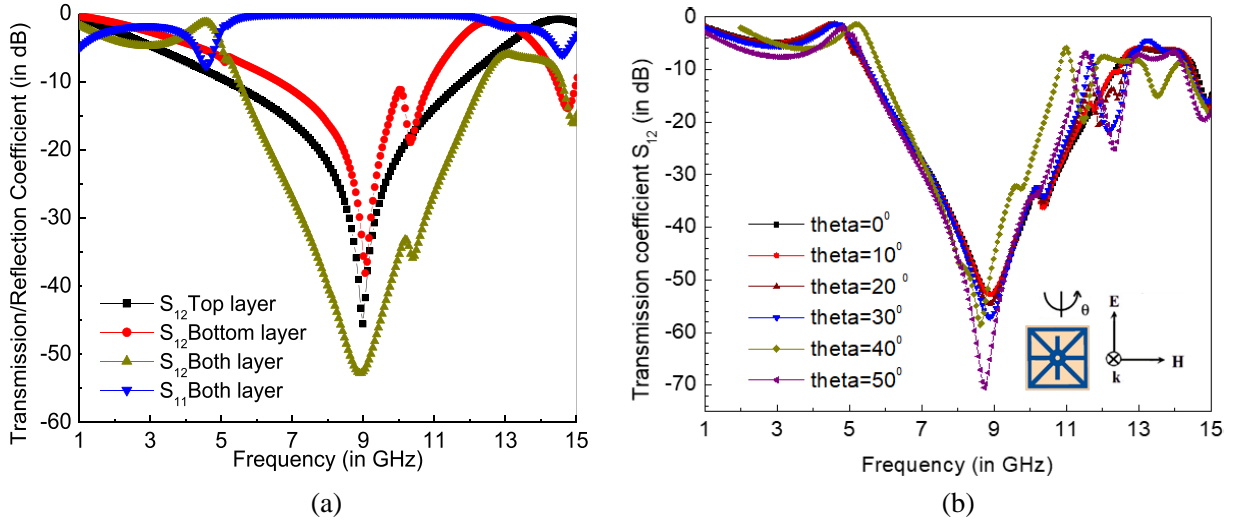

Figure 9. (a) Transmission/Reflection coefficient characteristics for the different layers of the proposed FSS for TE polarization, and (b) transmission coefficient characteristics under oblique incidence for TE polarization.

From the current distribution, the even (same current direction) and odd (opposite current direction) modes in the corresponding top and bottom FSS structure can be seen, and the coupling capacitances between the unit cells due to the periodic arrangement can be further evaluated. The stand-alone top layer FSS (SSR-PCC) acts as a band-stop filter in the frequency range 5–12 GHz and acts as a band-pass filter in the rest of the frequency range. The bottom layer FSS (SMRS-CP) acts as a band-stop filter in the frequency ranges 6.6–11 GHz and 14.4–15 GHz and acts as a bandpass filter in the rest of the frequency ranges. The equivalent circuit modelling in terms of transmission line is shown in Figure 12. From the equivalent circuit modelling the input impedance can be written as,

$$Z_{in} = Z_{\text{FSS1}} || Z_1 \tag{3}$$

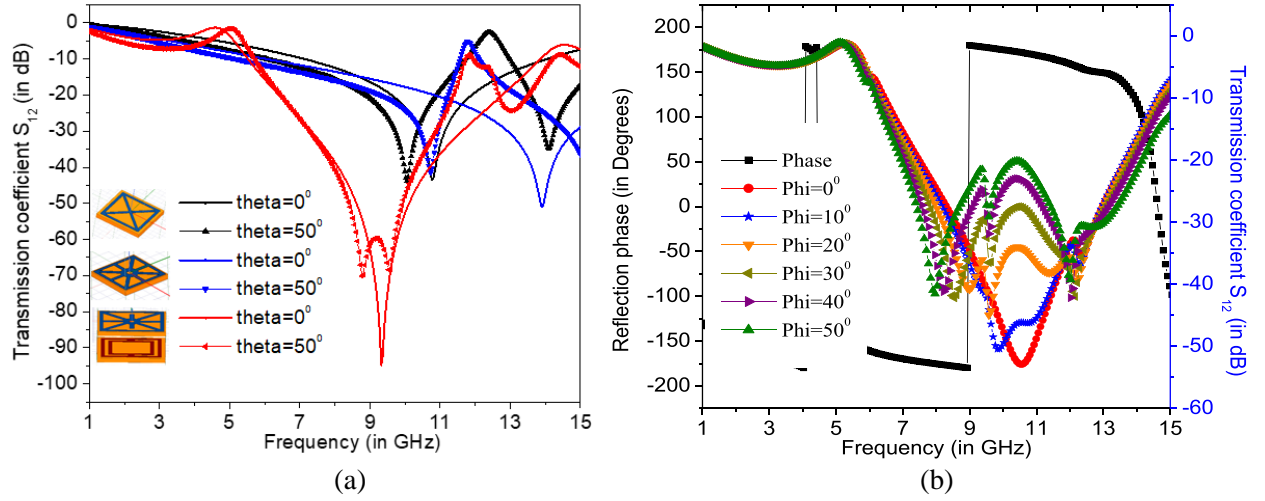$$Z_1 = \frac{Z_{d1}\left(Z_2 + jZ_{d1}\tan(\beta_1 t_{sub1})\right)}{Z_{d1} + jZ_2\tan(\beta_1 t_{sub1})} \tag{4}$$

Figure 10. Transmission coefficient characteristics versus frequency (a) for incidence angles $\theta = 0°$ and $\theta = 50°$ for different stages involved in the development of the FSS structure, and (b) for different polarization angles (TE polarization) along with reflection phase characteristics.
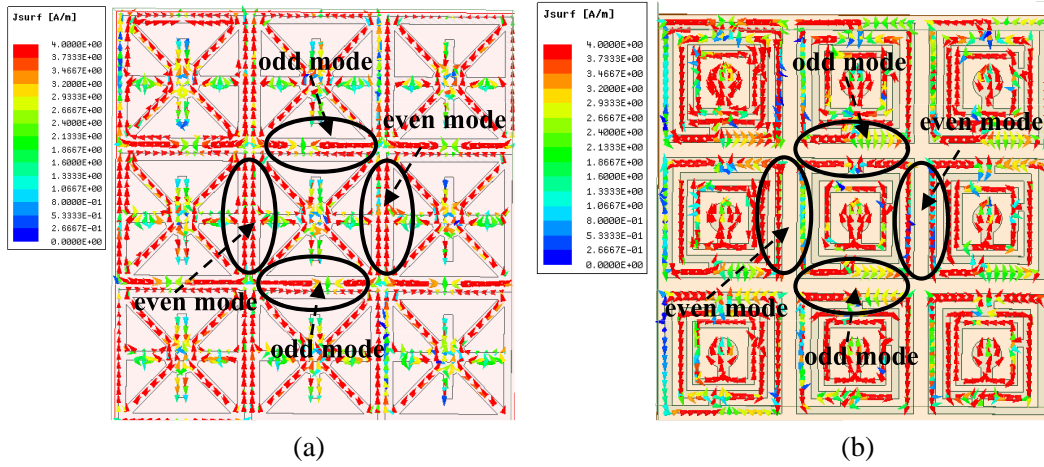

Figure 11. Simulated current distribution for (a) top and (b) bottom FSS layers.

$$Z_2 = \frac{Z_{\text{foam}}\left(Z_3 + jZ_{\text{foam}}\tan(\beta_{\text{foam}}t_{\text{foam}})\right)}{Z_{\text{foam}} + jZ_3\tan(\beta_{\text{foam}}t_{\text{foam}})} \tag{5}$$

$$Z_3 = Z_{\text{FSS2}}\|Z_4 \tag{6}$$

$$Z_4 = -jZ_{d2}\cot\left(\beta_2 t_{sub2}\right) \tag{7}$$

where $Z_0 = 377\,\Omega$, $Z_{di} = \frac{Z_0}{\sqrt{\varepsilon_{si}}}$, $\beta_i = \frac{2\pi\sqrt{\varepsilon_{si}}}{\lambda}$, where $i = 1, 2$. Z_i, ε_{si}, and β_i are the intrinsic impedance, dielectric constant, and phase constant of the ith transmission line section, respectively, and Z_{Foam} and β_{Foam} are the intrinsic impedance and phase constant of the foam [26–28] as detailed in Figure 12. For the proposed FSS structure, t_{sub1} and t_{sub2} are the thicknesses of the substrate, and since they are equal, Z_{d1} and Z_{d2} are also equal. To introduce an air gap ($\approx 3.2\,\text{mm}$) between two FSS layers, four short pillars of foam post have been introduced at four corners between two FSSs in fabricated prototype. The same has also been considered in the equivalent transmission line circuit model. The values of the lumped circuit parameters for Z_{FSS1} and Z_{FSS2} can also be extracted by using the methodology mentioned in [9].
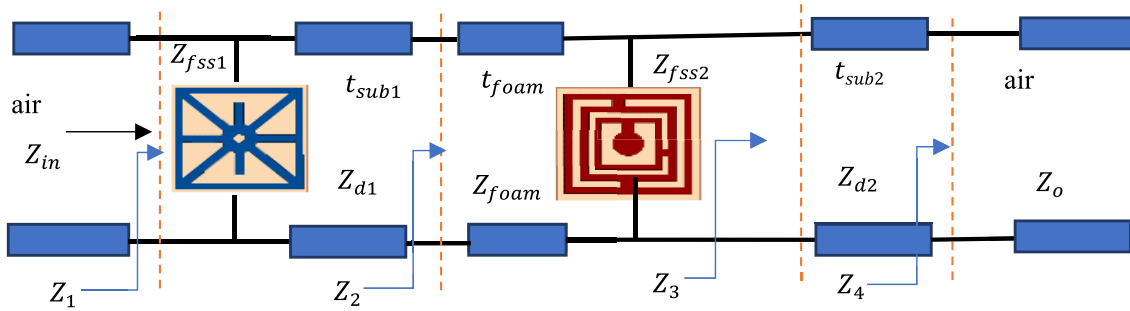
Figure 12. Simplified transmission line equivalent model of the FSS structure.

4. ANTENNA LOADED WITH FSS

The two layered FSS structure is introduced underneath the antenna geometry as shown in Figure 1(a). After introducing FSS underneath the antenna geometry, the impedance bandwidth ($S_{11} < -10$ dB) shifts slightly towards the higher side of the frequency spectrum (3.75–14.4 GHz as per simulation characteristic) with more prominent S_{11} minima at 5.5 GHz, 9.5 GHz, and 13.5 GHz as shown in Figure 13(a). There has been a considerable increase in the gain of the antenna over the wide operating bandwidth as shown in Figure 13(b) with the peak realized gain S_{11} reaching up to 7.5 dBi. The effect of the distance between the antenna and the FSS structure (t_{air}) on the S_{11} characteristics is shown in Figure 13(a). The height $t_{air} = 7$ mm is considered in the proposed structure as it gives the optimum results. The radiation efficiency over the band is varying from 73% to 93%. The rectangular plot at 9.5 GHz showing the co and cross polarization levels of both antenna and antenna loaded with FSS is plotted in Figure 14. The co polarization level of the antenna loaded with FSS is better than that of only antenna, and the cross polarization level of the antenna loaded with FSS is less than only antenna. The radiation characteristics of the antenna loaded with FSS have been plotted for the frequency points 4 GHz, 6 GHz, 9.5 GHz, and 13 GHz, in both $\Phi = 0°$ and $\Phi = 90°$ planes as shown in Figure 15. The antenna and FSS structures have been fabricated in house using the 'thermal toner transfer method' and shown in Figure 16. An in-house Vector Network Analyzer (VNA) (make: Anritsu, Model No: MS2028C VNA Master) has been used for taking the measurement of the scattering parameters of the prototype. The radiation characteristics have been measured using an in-house
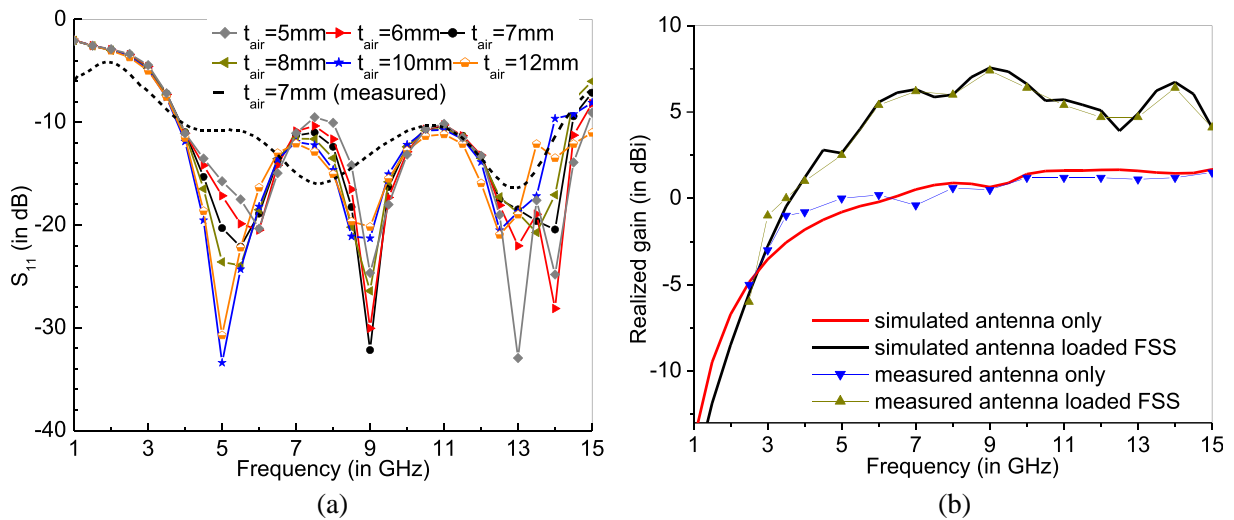

Figure 13. (a) S_{11} characteristics versus frequency for different heights between the antenna and FSS along with the measured result, and (b) peak realized gain for antenna only and antenna loaded with FSS.
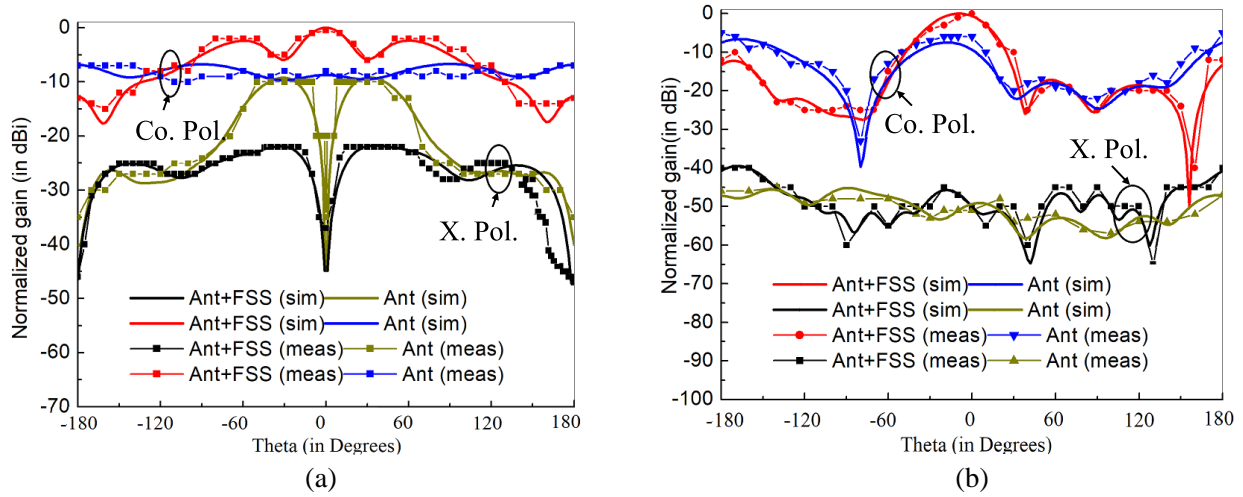
Figure 14. Simulated and measured rectangular radiation pattern for only antenna and antenna loaded with FSS at 9.5 GHz at (a) $\Phi = 0°$ and (b) $\Phi = 90°$.
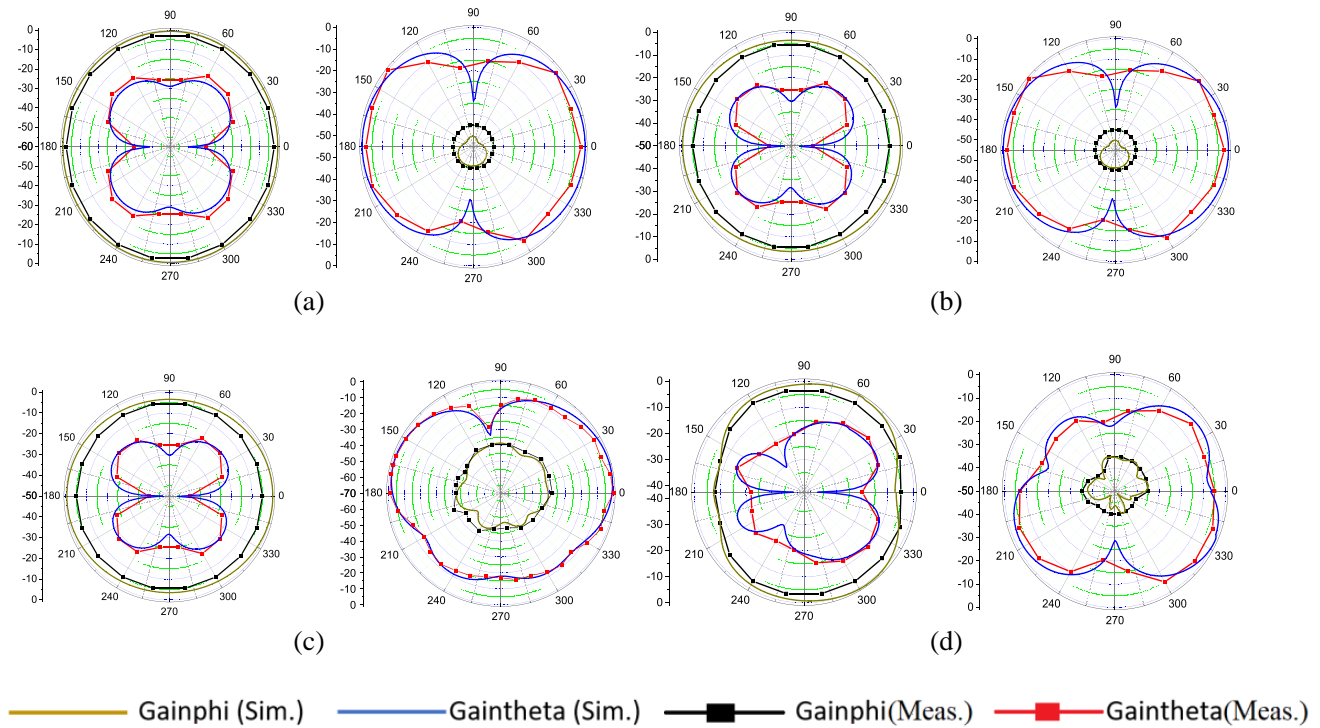

Figure 15. Simulated and measured radiation pattern for antenna loaded with FSS for $\Phi = 0°$ and at $\Phi = 90°$ (a) 4 GHz, (b) 6 GHz, (c) 9.5 GHz and (d) 13 GHz.

antenna measurement setup consisting of analog microwave signal generator (Make: Keysight, Model No: N5173B), standard gain horn antennas, motorized antenna unit, and USB power sensor (Make: Anritsu, Model No: MA24118A). The measured S_{11}, peak realized gain, and radiation patterns have been plotted along with the simulated results in Figures 13, 14, and 15. The FSS loaded antenna offers similar measured and simulated impedance bandwidths ($S_{11} \leq -10$ dB, SWR < 2) with variation in S_{11} characteristics over the band ($S_{11} \leq -10$ dB) due to the fabrication tolerances like characteristic of material used, soldering material, and imperfections in some connectors like commercial probe, SMA connectors which change the impedance characteristics of the prototype from simulated results.
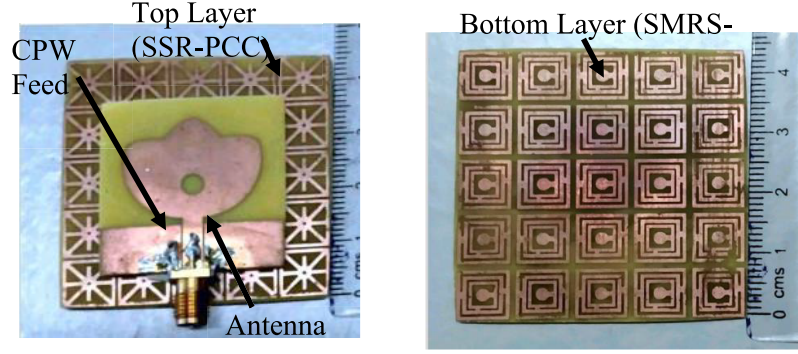
Figure 16. Fabricated FSS loaded antenna geometry.

Table 3. Comparison of the proposed antenna loaded FSS with other existing works.

Ref.	FSS dimension ($L \times W \times T$, in mm)	No. of Metamaterial/FSS layers	Dimension of antenna ($L \times W \times T$, in mm)	Bandwidth Antenna with FSS (in GHz)	Stability analysis (in degrees)	Gain enhancement (in dBi)
[29]	Not mentioned	Two (double sided)	Not mentioned	2.32–2.65, 5.2–5.89	Not given	3.69
[7]	$44 \times 44 \times 0.8$ (each layer)*	Two (stacked)	$35 \times 30 \times 0.8$	3.05–13.4	Not given	4
[5]	$110.25 \times 31.5 \times 1.6$	Three (side by side)	$112 \times 96.25 \times 1.6$, Cylindrical DRA height = 7.8	5.15–5.35, 5.4–5.65, 5.7–5.9	Not given	2
[6]	$45 \times 45 \times 3.2$	Single	$45 \times 40 \times 1.6$	2.18–3.04	Not given	5.76
[8]	$58 \times 58 \times 0.8$	Two (double sided)	$40 \times 30 \times 0.8$ DRA height = 4.3	7.6–12.2	40°	3.3
[9]	$45 \times 45 \times 0.254$ (each layer)*	Two (stacked)	$14.4 \times 23.3 \times 0.254$ annular ring shaped cylindrical DRA height = 3	3.75–14	40°	4.45
Proposed	$45 \times 45 \times 1.8$ (each layer)*	Two (stacked)	$31 \times 30 \times 1.8$	3.8–14.4	50°	5.9

* without considering thickness of air gap/foam material.

5. CONCLUSION

It can be concluded that the proposed two layered FSS geometry enhances the gain of the lotus shaped antenna significantly over the operating band. The FSS loaded antenna operates over 3.8 GHz to 14.4 GHz with peak realized gain of 7.5 dBi. It has been noticed that the multi-layered FSS structures can provide wideband response and better angular stability under oblique incidence. A comparative study has been done on the performance parameters of the proposed FSS loaded antenna with existing FSS loaded antenna geometries available in the literature and is presented in Table 3 which highlights the merits of the proposed FSS loaded bioinspired antenna in terms of compactness, ultra-wide operating bandwidth, and improved gain. The time domain analysis reveals the fact that 150 ps and 200 ps monocycle pulses are suitable for the proposed antenna. The proposed structure can be used as electromagnetic sensor for UWB applications.

ACKNOWLEDGMENT

REFERENCES

1. Narayan, S., B. Sangeetha, and R. M. Jha, *Frequency Selective Surfaces Based High Performance Microstrip Antenna*, Springer Briefs in Electrical and Computer Engineering, Springer, Singapore, 2016.

2. Munk, B. A., *Frequency Selective Surfaces: Theory and Design*, Wiley, New York, USA, 2005.

3. Sievenpiper, D., L. Zhang, R. F. J. Broas, N. G. Alexopolous, and E. Yablonovitch, "High-impedance electromagnetic surfaces with a forbidden frequency band," *IEEE Trans. Antennas Propag.*, Vol. 47, No. 11, 2059–2074, Nov. 1999.

4. Pan, W., C. Huang, P. Chen, X. Ma, C. Hu, and X. Luo, "A low-RCS and high-gain partially reflecting surface antenna," *IEEE Trans. Antennas Propag.*, Vol. 62, No. 2, 945–949, Feb. 2014.

5. Das, G., A. Sharma, R. K. Gangwar, and M. S. Sharawi, "Performance improvement of multiband MIMO dielectric resonator antenna system with a partially reflecting surface," *IEEE Antennas Wirel. Propag. Lett.*, Vol. 18, No. 10, 2105–2109, Aug. 2019.

6. Ameen, M. and R. K. Chaudhary, "Metamaterial-based wideband circularly polarised antenna with rotated V-shaped metasurface for small satellite applications," *Electron Lett.*, Vol. 55, No. 7, 365–366, Apr. 2019.

7. Kundu, S., A. Chatterjee, S. Kumar Jana, and S. K. Parui, "A compact umbrella-shaped UWB antenna with gain augmentation using frequency selective surface," *Radioengg.*, Vol. 27, No. 2, 448–454, Jun. 2018.

8. Bhattacharya, A., B. Dasgupta, and R. Jyoti, "Design and analysis of ultrathin X-band frequency selective surface structure for gain enhancement of hybrid antenna," *Int. J. RF Microw. Computer-Aided Engg.*, Vol. 31, No. 2, 1–12, Dec. 2020.

9. Bhattacharya, A., B. Dasgupta, and R. Jyoti, "A simple frequency selective surface structure for performance improvement of ultra-wideband antenna in frequency and time domains," *Int. J. RF Microw. Computer-Aided Engg.*, Vol. 31, No. 11, 1–13, Dec. 2021.

10. Balanis, C. A., *Antenna Theory Analysis and Design*, John Wiley and Sons, New Jersey, 2005.

11. Gielis, J., "A generic geometric transformation that unifies a wide range of naturaland abstract shapes," *American J. Botany*, Vol. 90, No. 3, 333–338, 2003.

12. Chattopadhyay, S., *Trends in Research on Microstrip Antennas*, IntechOpen, London, UK, 2017.

13. Mighani, M. and M. Akbari, "New UWB monopole planer antenna with dual band notched," *Progress In Electromagnetics Research C*, Vol. 52, 153–162, 2014.

14. Li, H. F., Z. N. Chen, and L.-W. Li, "Investigation of time-domain characteristics of thin-wire antennas," *Microw. Opt. Techn. Lett.*, Vol. 43, No. 3, 253–258, Nov. 2004.

15. Sarkar, T. K., D. Ghosh, A. De, M. C. Taylor, M. C. Wicks, and E. L. Mokole, "Transmission and reception by ultra-wideband (UWB) antennas," *IEEE Antennas Propag. Mag.*, Vol. 48, No. 5, 67–99, Oct. 2006.

16. Ganguly, D., D. Guha, S. Das, and A. Rojatkar, "Systematic approach to estimating monocycle pulse for time-domain studies of UWB antennas using numerical computations and simulation tools," *IEEE Antennas Propag. Mag.*, Vol. 56, No. 4, 73–87, Aug. 2014.

17. Ansys High Frequency Structural Simulator (HFSS). Version 16.2.

18. Computer Simulation Software (CST). Version 2018.

19. Antony, A. and B. Dasgupta, "Lotus shaped printed antenna for UWB applications," *2021 IEEE 18th India Council Int. Conf. (INDICON)*, Guwahati, India, Feb. 2021.

20. Schantz, H. G., *The Art and Science of Ultrawideband Antennas*, Artech House, Norwood, MA, 2005.

21. Zahran, S. R., M. A. Abdalla, and A. Gaafar, "Time domain analysis for foldable thin UWB monopole antenna," *AEU-Inter. J. of Electro. Comm.*, Vol. 83, 253–262, 2018.

22. Valderas, D., J. I. Sancho, D. Puente, C. Ling, and X. Chen, *Ultrawideband Antennas Design and Applications*, Imperial College Press, London, 2011.

23. Chen, Z. N., X. H. Wu, H. F. Li, N. Yang, and M. Y. W. Chia, "Considerations for source pulses and antennas in UWB radio systems," *IEEE Trans. Antennas Propag.*, Vol. 52, No. 7, 1739–1748, Jul. 2004.

24. Natarajamani, S., "Some studies on designs of planar antennas for UWB applications," Ph.D. dissertation, Dept. Elect. and Comm. Eng., NIT Rourkela, Odisha, India, 2014.

25. Kwon, D. H., "Effect of antenna gain and group delay variations on pulse-preserving capabilities of ultrawideband antennas," *IEEE Trans. Antennas Propag.*, Vol. 54, No. 8, 2208–2215, Aug. 2006.

26. Costa, F., A. Monorchio, and G. Manara, "Efficient analysis of frequency selective surface by a simple equivalent-circuit model," *IEEE Antennas Wirel. Propag. Mag.*, Vol. 54, No. 4, 35–48, Sep. 2012.

27. Chatterjee, A. and S. K. Parui, "A triple-layer dual-bandpass frequency selective surface of third order response with equivalent circuit analysis," *Int. J. RF Microw. Computer Aided Engg.*, Vol. 30, No. 6, 1–7, Feb. 2020.

28. Ghosh, S., S. Bhattacharyya, and K. V. Srivastava, "Design, characterization and fabrication of a broadband polarization-insensitive multi-layer circuit analogue absorber," *IET Microw. Antennas Propag.*, Vol. 10, No. 8, 850–855, Jun. 2016.

29. Roy, S. and U. Chakraborty, "Gain enhancement of a dual-band WLAN microstrip antenna loaded with diagonal pattern metamaterials," *IET Comm.*, Vol. 12, No. 12, 1448–1453, Jun. 2018.